Electronic Supplementary Information (ESI)

Ta_3N_5-nanorods enabling highly efficient water oxidation via advantageous light harvesting and charges collection

Yuriy Pihosh[a], Tsutomu Minegishi[a], Vikas Nandal[b], Tomohiro Higashi[c], Masao Katayama[c], Taro Yamada[c], Yutaka Sasaki[c], Kazuhiko Seki[b], Yohichi Suzuki[d], Mamiko Nakabayashi[e], Masakazu Sugiyama[a], and Kazunari Domen*[f]*

[a] *Research Center for Advanced Science and Technology, The University of Tokyo, 4-6-1, Komaba, Meguro-ku, Tokyo 153-8904, Japan*

[b] *Nanomaterials Research Institute, National Institute of Advanced Industrial Science and Technology, 1-1-1 Higashi, Tsukuba, Ibaraki 305-8565, Japan*

[c] *Department of Chemical System Engineering, School of Engineering, The University of Tokyo, 7-3-1 Hongo, Bunkyo-ku, Tokyo 113-8656, Japan*

[d] *Quantum Computing Center, Keio University,3-14-1 Hiyoshi, Kohoku-ku, Yokohama, Kanagawa, 223-8522, Japan*

[e] *Institute of Engineering Innovation, The University of Tokyo, 2-11-16 Yayoi, Bunkyo-ku, Tokyo 113-8656, Japan*

[f] *University Professors Office, The University of Tokyo, 7-3-1 Hongo, Bunkyo-ku, Tokyo 113-8656, Japan*

*Corresponding authors, email: domen@chemsys.t.u-tokyo.ac.jp, pihosh_y@enesys.rcast.u-tokyo.ac.jp

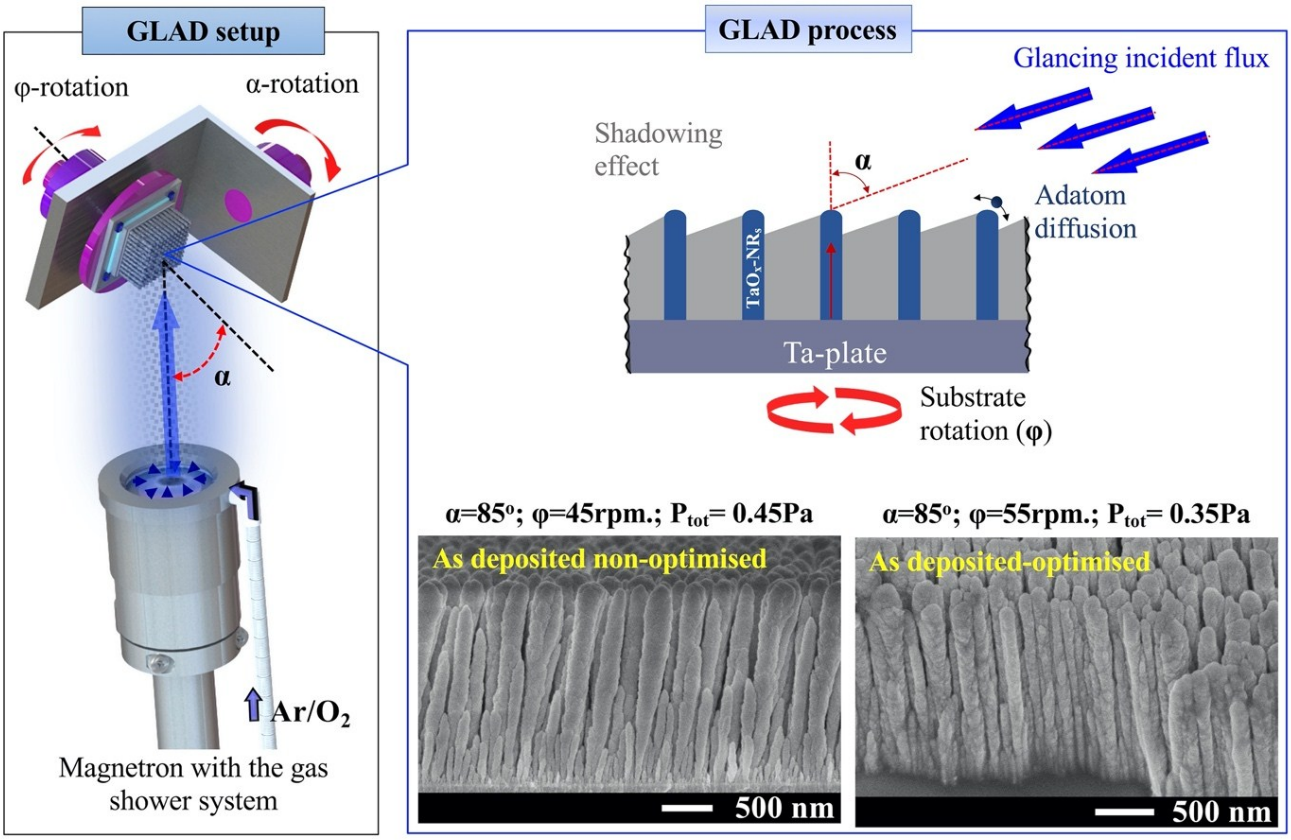

Figure S1. Schematic illustration of the fabrication of TaO_x-NRs by the Glancing Angle Deposition technique.

The fabrication of uniform TaO_x-nanorods were performed in a custom-made magnetron Glancing Angle Deposition (GLAD) system, which was equipped with a three-dimensional rotation stage that allowed positioning of the substrates over the magnetron at a desired distance and normal or glancing angle. In such a GLAD configuration, the deposition under the glancing angle led to the formation of vertically standing separated nanorods, instead of a thin compact film, owing to the shadowing effect and limited ad-atoms diffusion[1–4], which prevented the deposition of incident atoms behind spontaneously formed islands, see **Fig. S1**. Prior to the fabrication process, the GLAD equipment was evacuated by turbomolecular pumps to a base pressure of ~ 6×10^{-4} Pa. Tantalum (Ta) plates (10 × 10 × 0.3mm, 99.95%, Nilaco Co., mirror polished) were located over the magnetron source with the Ta target (99.99%, Toshima Co.) at the glancing deposition angle $\alpha = 85°$ to the substrate normal. A mixture of Ar/O_2 (15 sccm/7.5 sccm) gases was used for the reactive sputtering of TaO_x at a total pressure of ~0.45 Pa or/and 0.35 Pa. After setting all required GLAD parameters, pre-sputtering was performed for 15 minutes at 350 W with a closed magnetron shutter. When the deposition rate of sputtered material reached a constant rate, shutter was opened, and the GLAD process was started with a sample rotation speed (ϕ-rotation) of 45 rpm or/and 55 rpm. Owing to the shadowing effect and the limited diffusion of adatoms, the morphology of the growing film broke to be columnar while a continuous substrate rotation directed the formation of the well-separated and uniform TaO_x-NRs to vertically stand on the substrate. We performed a series of experiments to determine the experimental parameters needed to fabricate uniform and well-separated TaO_x-NRs by the GLAD technique. The morphology of the nanorods was dependent on many factors involving the material and deposition condition, such as substrate roughness, angular distribution of the deposited flux, working gas pressure and flux energetics. However, it was accepted that there was a fixed relation between the angular distribution of flux and the working gas pressure. At a higher working pressure, there were more collisions between the sputtered atoms, which significantly changed the flux distribution and resulted in a negative effect on the diameter of the fabricated nanorods and their density on the substrate during the GLAD process. In the case of constant experimental parameters, such as working pressure and power (in our case R.F magnetron power), the flux energetics will reach a thermal equilibrium state at a desired distance with a constant deposition rate of deposited atoms. The energy flux increases with decreasing the working pressure owing to the higher electrons temperature[5]. Thus, determination of the most appropriate deposition distance (distance from the sputtered source to the substrate), working pressure and substrate rotation speed is very important to fabricate the required nanostructure. In our case, the deposition distance was fixed to 12 cm, and the Rf magnetron power was 350 W. By optimization of the GLAD parameters, such as magnetron power, working pressure and sample rotation speed, we were able to optimise the diameter and areal density of the nanorods. The sample with well-separated and uniform shaped nanorods as well as vertical alignment is denoted in this work as “optimised”, while the other sample, which consisted of a non-uniform NRs-shape, is denoted as “non-optimised”, as shown in **Fig. S1**. The optimised GLAD parameters (such as working pressure P_{tot}, glancing deposition angle α and sample rotation speed ϕ) are shown in the upper SEM images in **Fig. S1**.

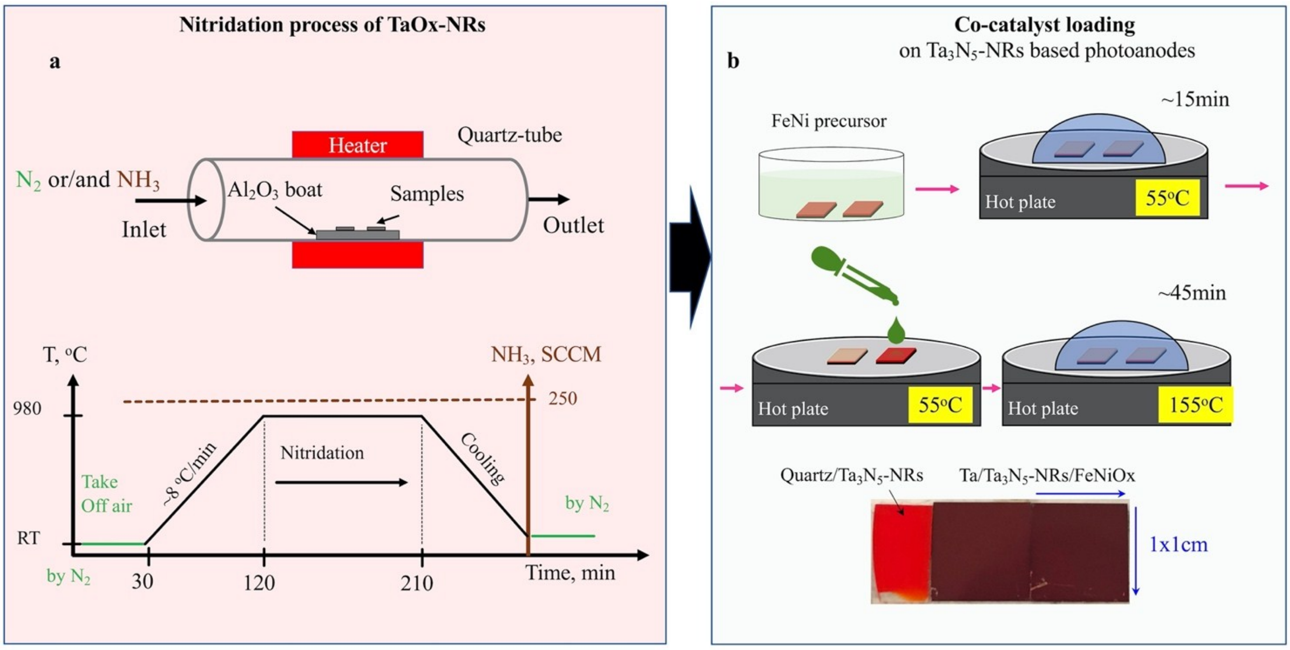

Figure S2. Schematic illustration of the nitridation process of TaO_x-NRs and co-catalyst loading on Ta/Ta_3N_5-NRs-based photoanodes

(a) Nitridation process. The as-grown amorphous TaO_x-nanorods on a Ta plates or/and quartz plates by GLAD were converted to the crystalline phase by nitridation in a horizontal tube furnace. At first, the fabricated samples were placed on an alumina boat and loaded to the quartz tube and then gas lines were connected to the tube by using air-tight flanges. The tube with the loaded samples was purged by nitrogen (N_2) gas (flow rate 250 sccm) for ~20 minutes to get rid of the air. Ammonia (NH_3) gas was introduced to the tube under a flow rate of 250 sccm and the flow of N_2 gas was stopped. After 10 minutes of a continuous flow of NH_3, we started heating the samples with a temperature ramping rate of ~8 deg min^{-1}. Samples were nitridised for 2.5 hours at 980 °C, followed by natural cooling at the same flow rate of NH_3. When the temperature in the nitridation furnace dropped to 25 ^oC, the flow of NH_3 gas was stopped, and N_2 gas was introduced again (at 250 sccm for ~15 min) to remove residual NH_3 before removing the samples.

(b) $FeNiO_x$ co-catalyst loading on Ta_3N_5 nanorods. A nitridised nanostructured Ta/Ta_3N_5-NRs-based photoanode was homogeneously covered by a FeNiOx co-catalyst immediately after the nitridation process by the following procedure. A freshly made solution of 20 mM $Ni(NO_3)_2{\times}6H_2O$ and 20 mM $(FeNO_3)_2{\times}9H_2O$ was mixed with a ratio of 1:1 and then stirred for 15 min under ambient conditions. Then, the Ta/Ta_3N_5-NRs-based photoanode was immersed in this precursor for 10 minutes and placed on a hot plate (at room temperature) and the samples were covered by a ceramic cap. This was followed by the heating of the modified samples at 55 °C in air for 15 min under the cap. Then, a few drops of the co-catalyst precursor were put on the preheated samples (until its surface was homogeneously covered by precursor) and the samples were covered again by the ceramic cap. This was followed by heating to 145 °C in air for 45 min. Subsequently, the samples were rinsed with milli-Q water to remove any residual precursors, followed by drying the samples under a N_2 steam. After electrical contact fabrication on the photoanode and encapsulation with epoxy (Araldide), the working area of the photoanodes was ~0.25–0.35 cm^{-2}.

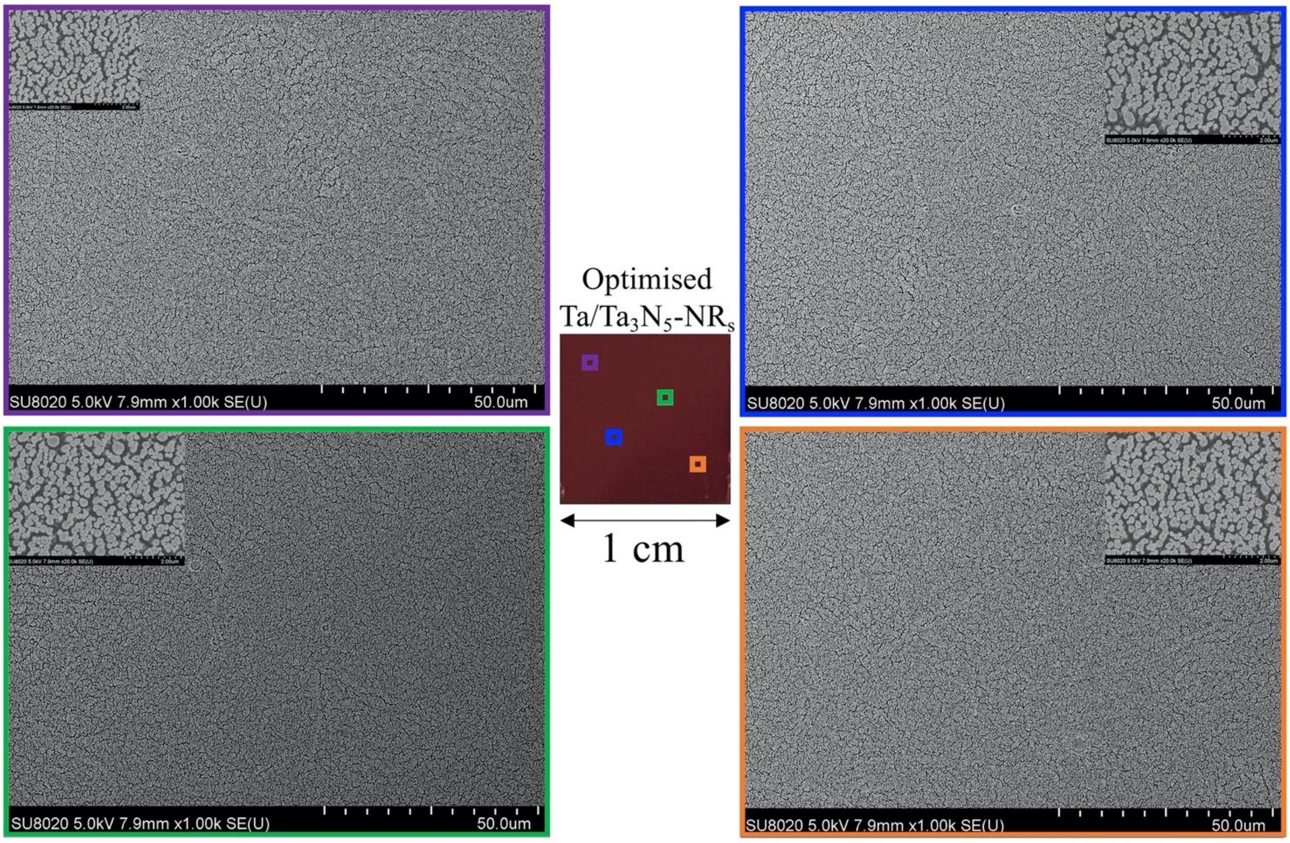

Figure S3. Low-magnification SEM images at different location of the optimised Ta$_3$N$_5$-NRs sample. The results indicate that the fabricated Ta$_3$N$_5$-NRs are uniformly distributed on the Ta substrate.

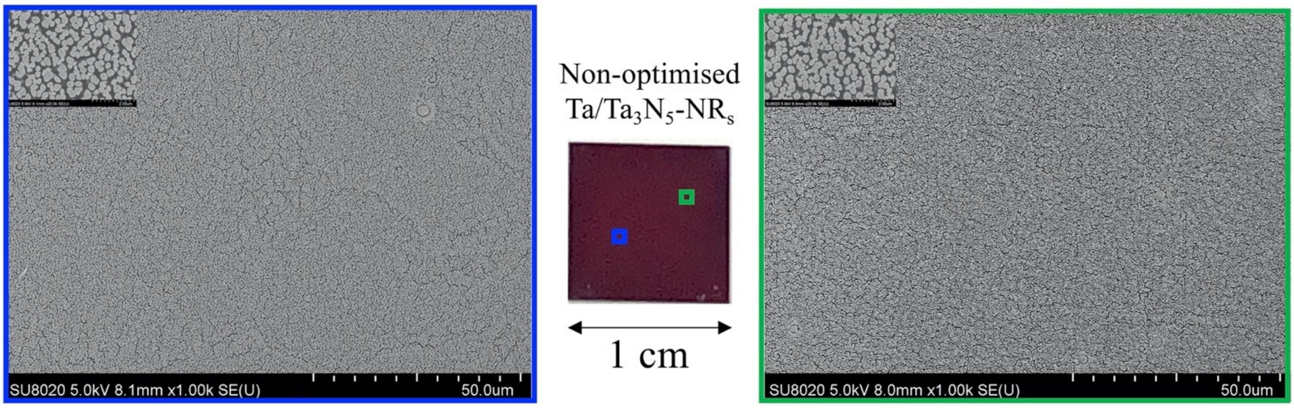

Figure S4. Low-magnification SEM images at different location of the non-optimised Ta_3N_5-NRs sample showing uniformly distribution of NRs.

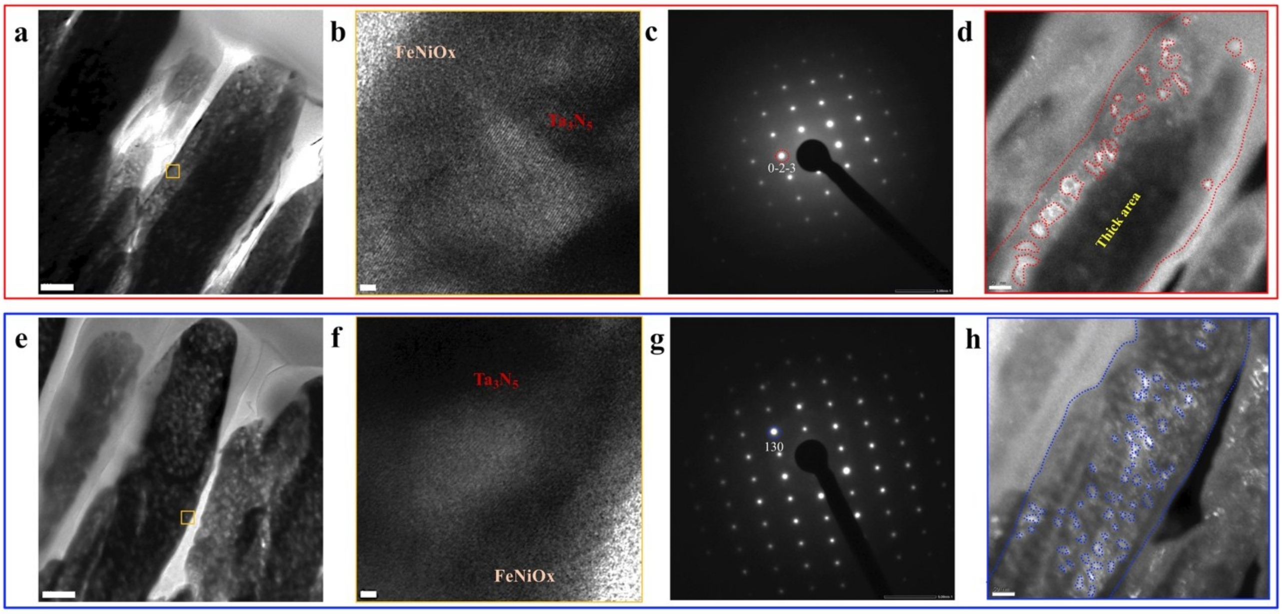

Figure S5. Transmission electron microscopy (TEM) analysis for the optimised and non-optimised Ta_3N_5-NRs/$FeNiO_x$-based photoanodes. High resolution transmission electron microscopy images of optimised (a–b) and non-optimised (e–f) Ta_3N_5-NRs taken along the [-3-32] and [-312] zone axes, respectively. (c and g) Selected area electron diffraction patterns acquired from the optimised (a) and non-optimised (e) Ta_3N_5-NRs. Dark field images for the optimised (d) and non-optimised (h) Ta_3N_5-NRs obtained from the (0-2-3) and (130) diffraction spots, respectively. Scale bars, (a, e) 100 nm, (b, f) 2 nm and (d, h) 50 nm.

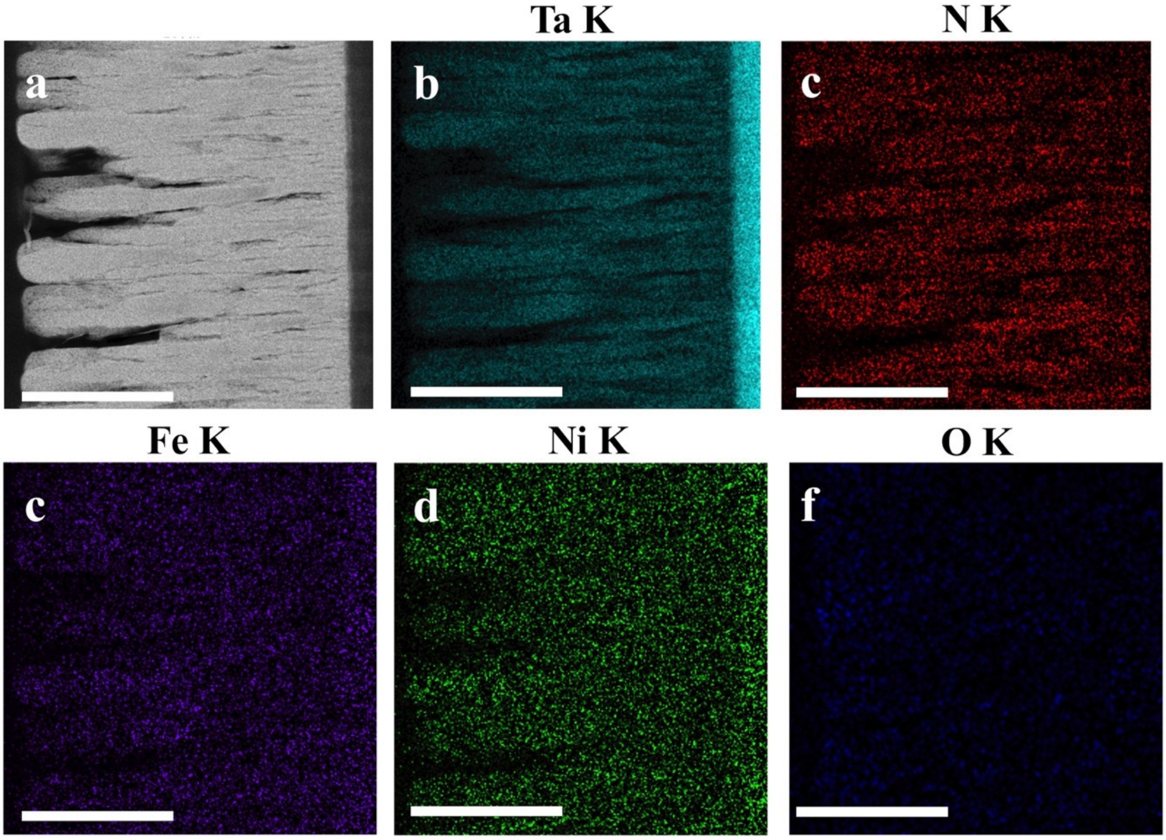

Figure S6. STEM-EDS analyses for optimised Ta/Ta_3N_5-NRs/$FeNiO_x$. (a) TEM cross-sectional view image of the Ta_3N_5-NRs/$FeNiO_x$ photoanode. STEM-EDS elemental mapping of the area in (a) for Ta, N, Fe, Ni and O. The cross-sectional elemental STEM-EDS mapping confirmed the uniform distribution of the $FeNiO_x$ co-catalyst elements of Fe and Ni on the Ta_3N_5-NRs surface.

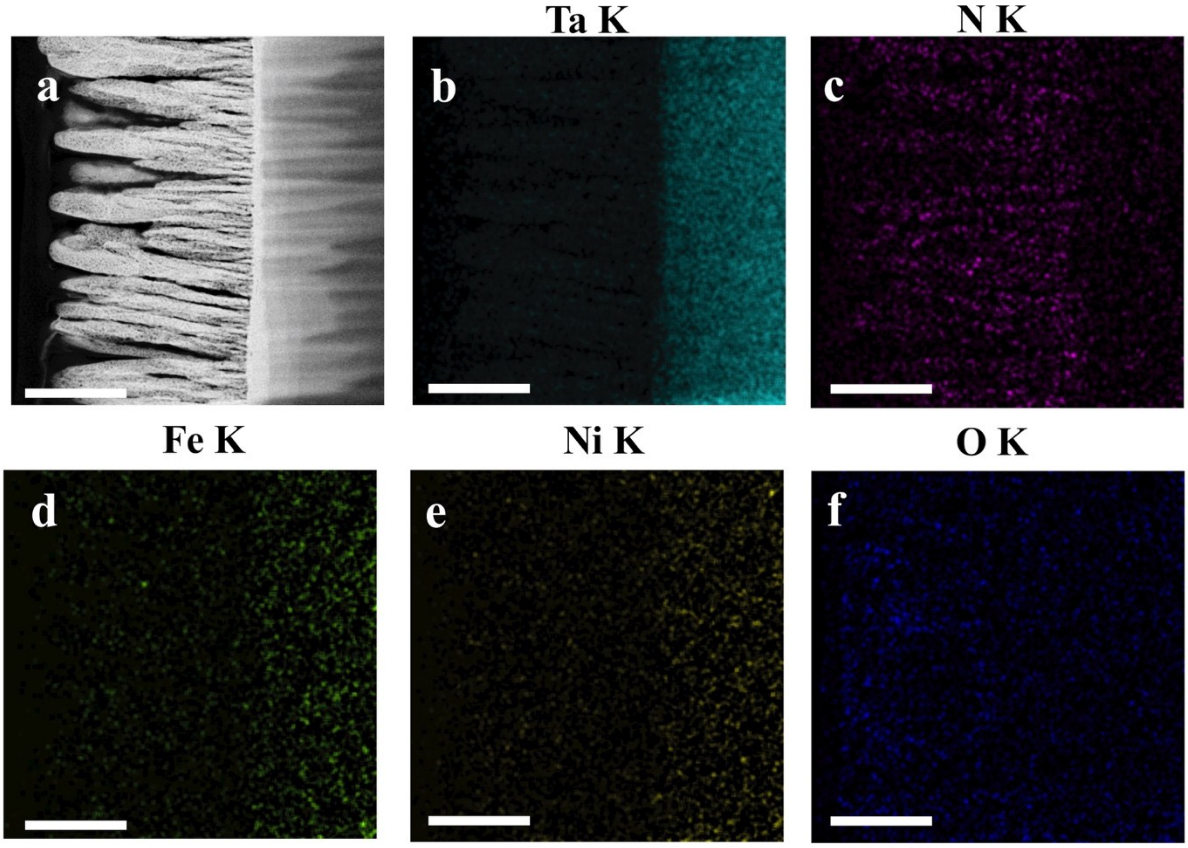

Figure S7. STEM-EDS analyses for non-optimised Ta/Ta_3N_5-NRs/$FeNiO_x$. (a) TEM cross-sectional view image of Ta_3N_5-NRs/$FeNiO_x$ photoanode. STEM-EDS elemental mapping of the area in (a) for Ta, N, Fe, Ni and O. The cross-sectional elemental STEM-EDS mapping confirmed the uniform distribution of the $FeNiO_x$ co-catalyst elements of Fe and Ni on the Ta_3N_5-NRs surface.

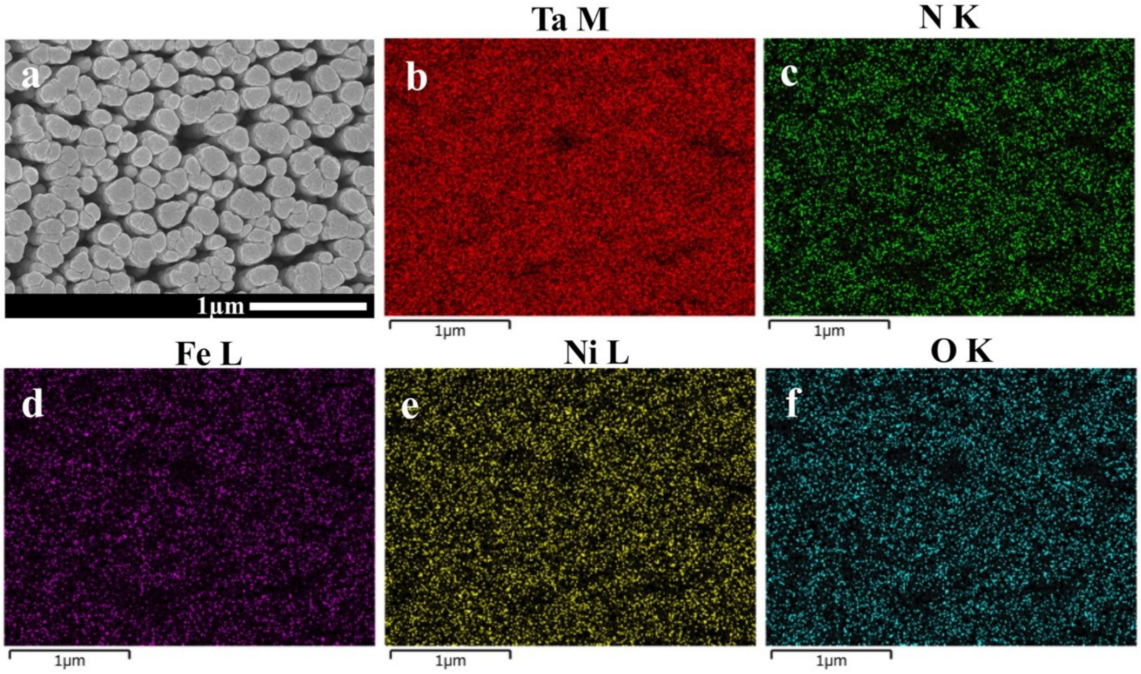

Figure S8. EDS analyses of optimised Ta/Ta_3N_5-NRs/$FeNiO_x$. (a) SEM top view image of Ta_3N_5-NRs/$FeNiO_x$ photoanode. EDS elemental mapping of the area in (a) for Ta, N, Fe, Ni and O. The elemental EDS mapping confirmed the uniform distribution of the $FeNiO_x$ co-catalyst elements of Fe and Ni on the Ta_3N_5-NRs surface.

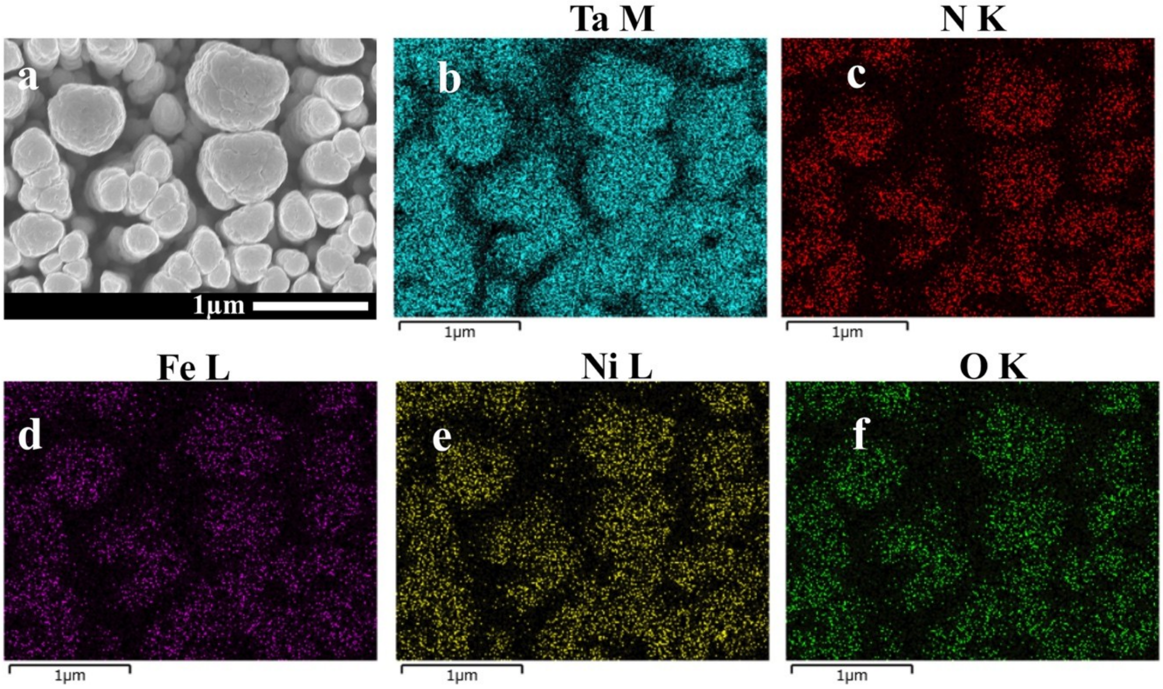

Figure S9. EDS analyses of non-optimised Ta/Ta_3N_5-NRs/$FeNiO_x$. (a) SEM top view image of Ta_3N_5-NRs/$FeNiO_x$ photoanode. EDS elemental mapping of the area in (a) for Ta, N, Fe, Ni and O. The elemental EDS mapping confirmed the uniform distribution of the $FeNiO_x$ co-catalyst elements of Fe and Ni on the Ta_3N_5-NRs surface.

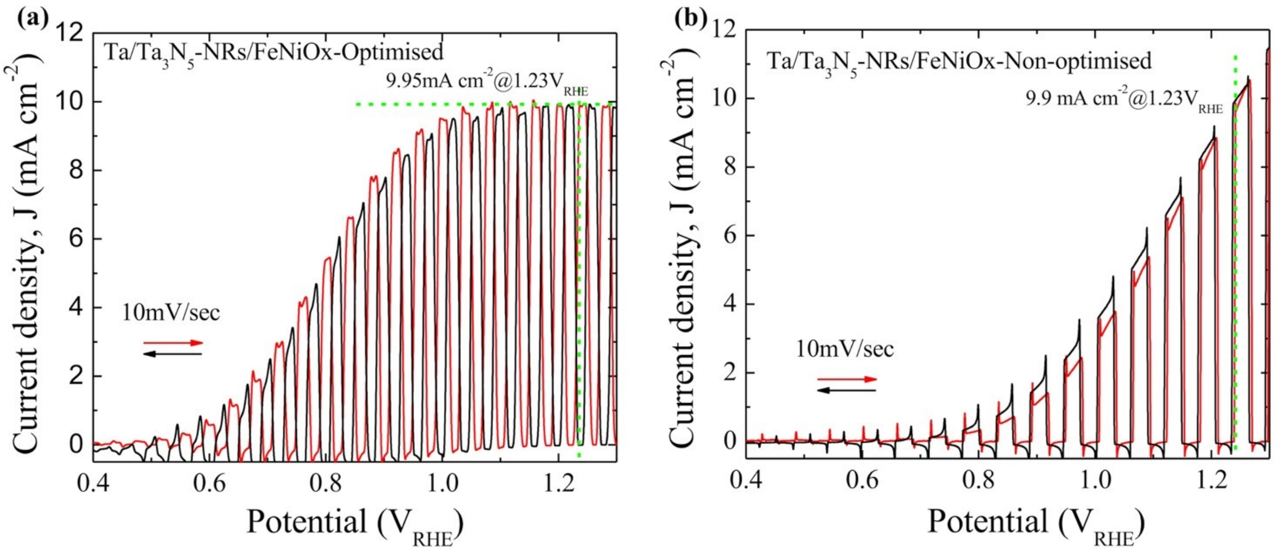

Figure S10. Photoelectrochemical properties of Ta_3N_5-NRs/$FeNiO_x$-based photoanodes. The photocurrent versus voltage (J–V_{RHE}) curves of Ta/Ta_3N_5-NRs/$FeNiO_x$-based photoanodes measured under chopped AM1.5G solar simulated light, (a) optimised and (b) non-optimised nanostructure. J–V_{RHE} curves were recorded in the anodic and cathodic directions at a scan rate of 10 mV s^{-1}.

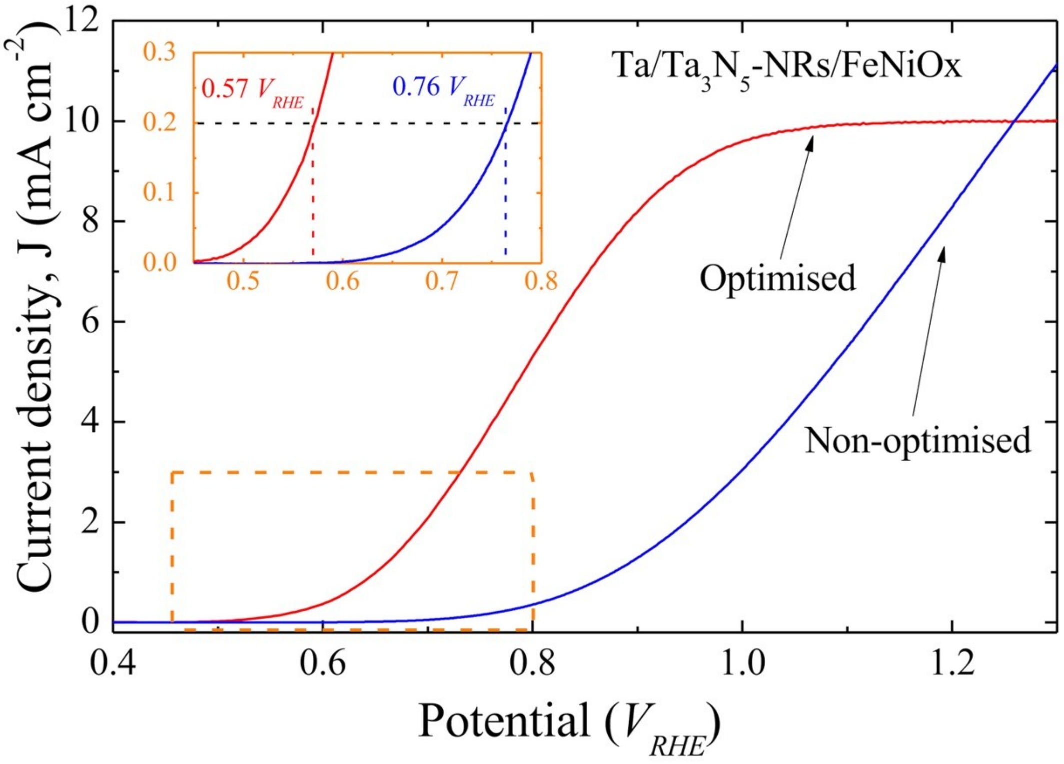

Figure S11. Onset potential definition for both the optimised and non-optimised Ta_3N_5-NRs-based photoanodes. The current-voltage (J–V_{RHE}) characteristics for both photoanodes were recorded in 1 M KH_2PO_4 (adjusted to pH 13 by KOH) under 1 sun of the simulated solar light at a scan rate of 10 mV s^{-1}. Inset figure corresponds to the zoomed J–V_{RHE} curves to clearly identify the onset potential at a measured photocurrent density value of 0.2 mA cm^{-2}. Onset potential for the optimised photoanode is 0.57 V_{RHE} and for the non-optimised is 0.76 V_{RHE}.

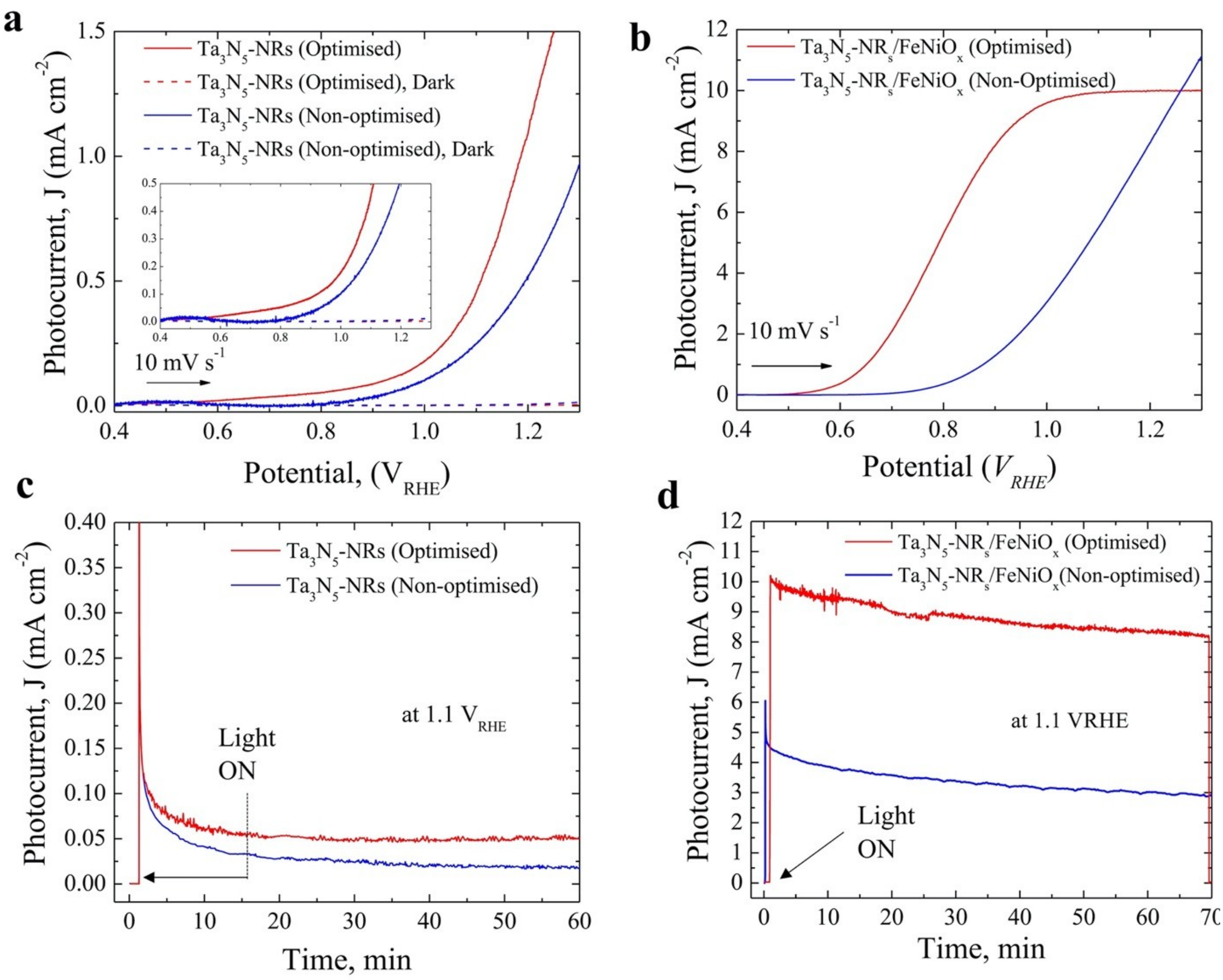

Figure S12. PEC performance of the optimised and non-optimised photoanodes with and without FeNiO$_x$ co-catalyst. Photocurrent versus voltage (J–V_{RHE}) curves of the optimized and non-optimized (a) Ta_3N_5-NR$_s$ and (b) Ta_3N_5-NR$_s$-NRs/FeNiO$_x$ photoanodes. Chronoamperometry characteristics of the optimized and non-optimized (c) Ta_3N_5-NRs and (d) Ta_3N_5-NR$_s$-NR$_s$/FeNiO$_x$ photoanodes at 1.1V_{RHE}.

The all curves were measured at standard 3-electrodes configuration PEC cell under solar simulated light AM 1.5G in electrolyte of 1 M KH_2PO_4 adjusted to pH 13 by KOH.

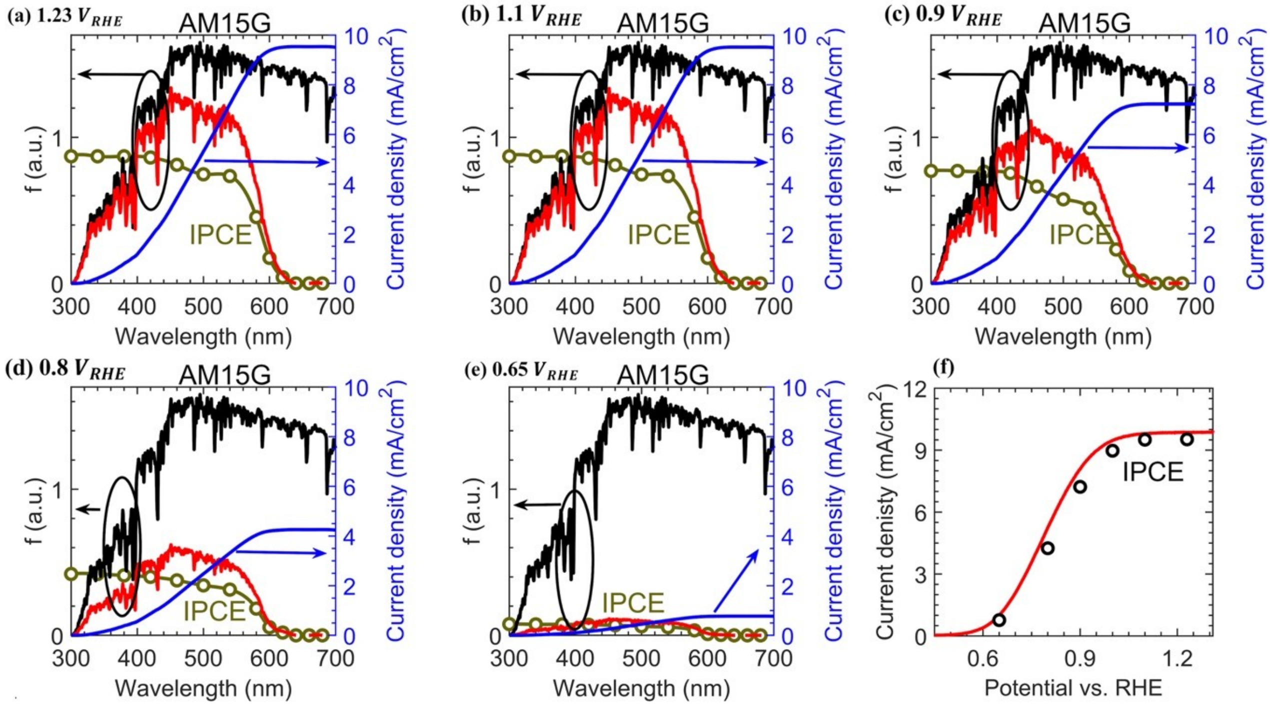

Figure S13. Incident photon-to-current efficiencies (IPCEs) of the optimised Ta_3N_5-NRs/$FeNiO_x$-based photoanode. (a)–(e) IPCE spectra (left Y-axis) of the optimised photoanode at different applied potentials V versus (RHE) and (right Y-axis) theoretical photocurrent obtained by integrating the product of IPCE with the AM1.5G (ASTM G173-03). (f) *J*–V_{RHE} characteristics of the optimised photoanode measured under solar simulated light with the plotted theoretical photocurrent from IPCEs integration (blue circle). The electrolyte used is 1 M KH_2PO_4 adjusted to pH 13 by KOH.

The theoretical photocurrent obtained by integrating the product of the IPCEs (measured at different V_{RHE}) with the AM1.5G photon flux over all wavelengths is close to the experimental value at the same V_{RHE}, thus IPCE and *J*–V_{RHE} data are in a good agreement.

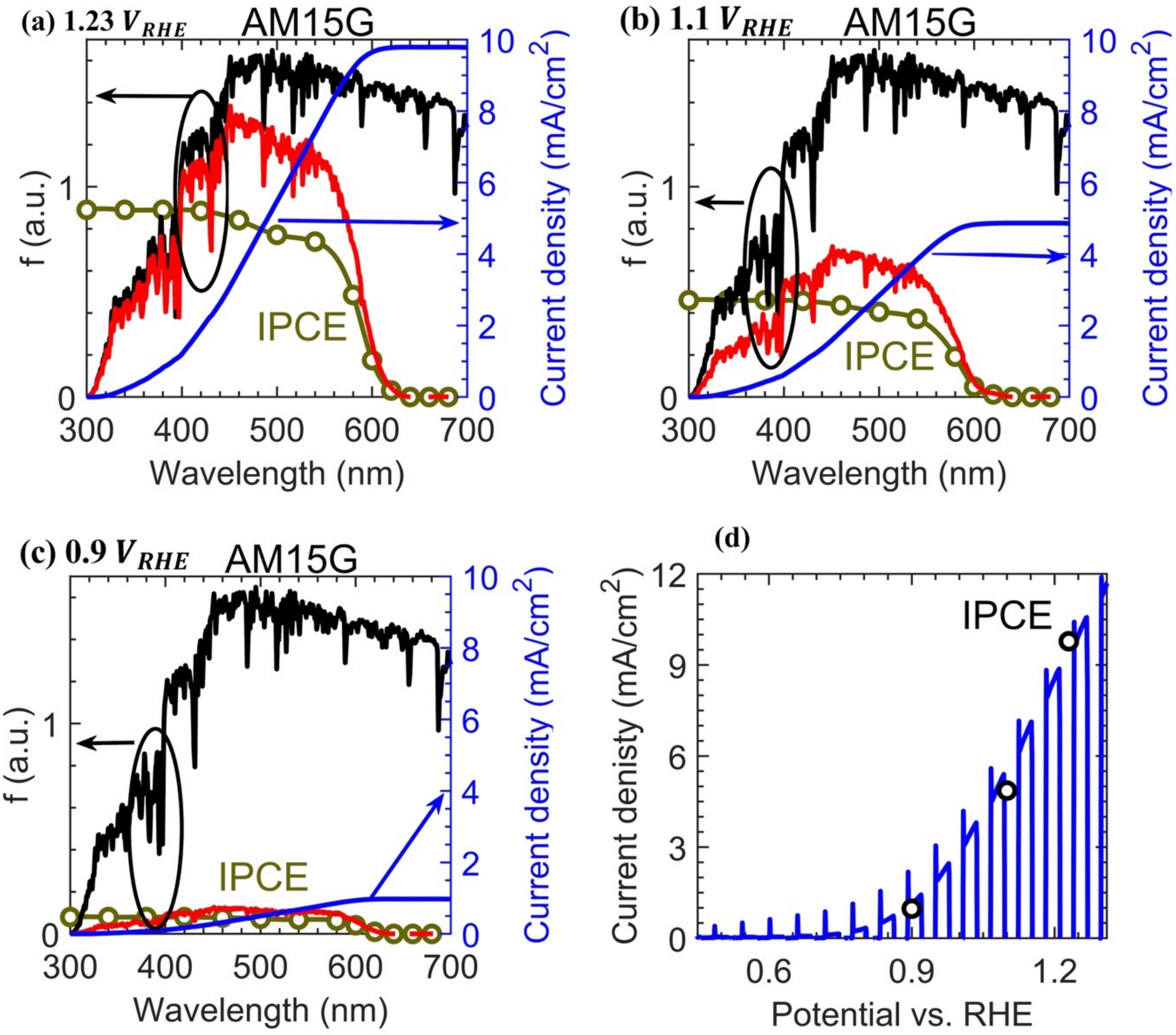

Figure S14. Incident photon-to-current efficiencies (IPCEs) of the non-optimised Ta_3N_5-NRs/FeNiO$_x$-based photoanode. (a)–(c) IPCEs spectra (left Y-axis) of the non-optimised photoanode at different applied potentials V versus (RHE) and (right Y-axis) theoretical photocurrent obtained by integrating the product of IPCE with the AM1.5G (ASTM G173-03). (d) J–V_{RHE} characteristic of the non-optimised photoanode measured under solar simulated light with the plotted theoretical photocurrent from IPCEs integration (blue circle). The electrolyte used is 1 M KH_2PO_4 adjusted to pH 13 by KOH.

The theoretical photocurrent obtained by integrating the product of the IPCEs (measured at different V_{RHE}) with the AM1.5G photon flux over all wavelengths is close to the experimental value at the same V_{RHE}, thus IPCE and J–V_{RHE} data are in a good agreement.

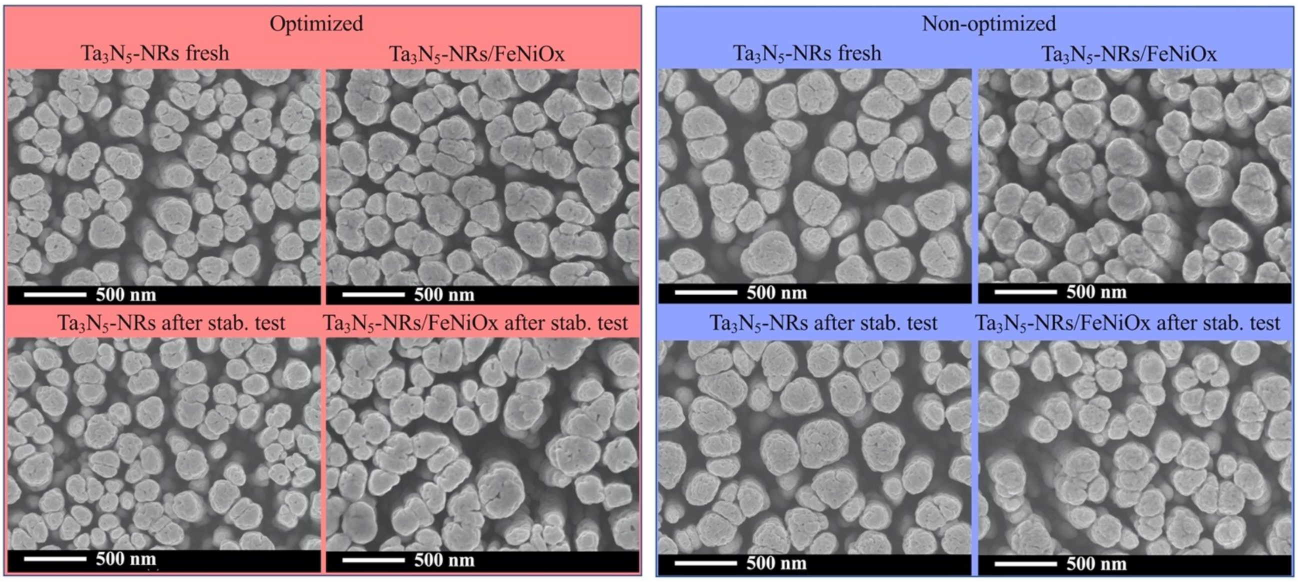

Figure S15. The SEM images of the both optimised and non-optimised Ta_3N_5-NRs based samples, including fresh ones and after PEC stability test at $1.1V_{RHE}$

The SEM images of both samples reveals that the morphology of NRs is retained after stability test of the samples with and without cocatalyst which suggest that the NRs do not undergo photocorrosion.

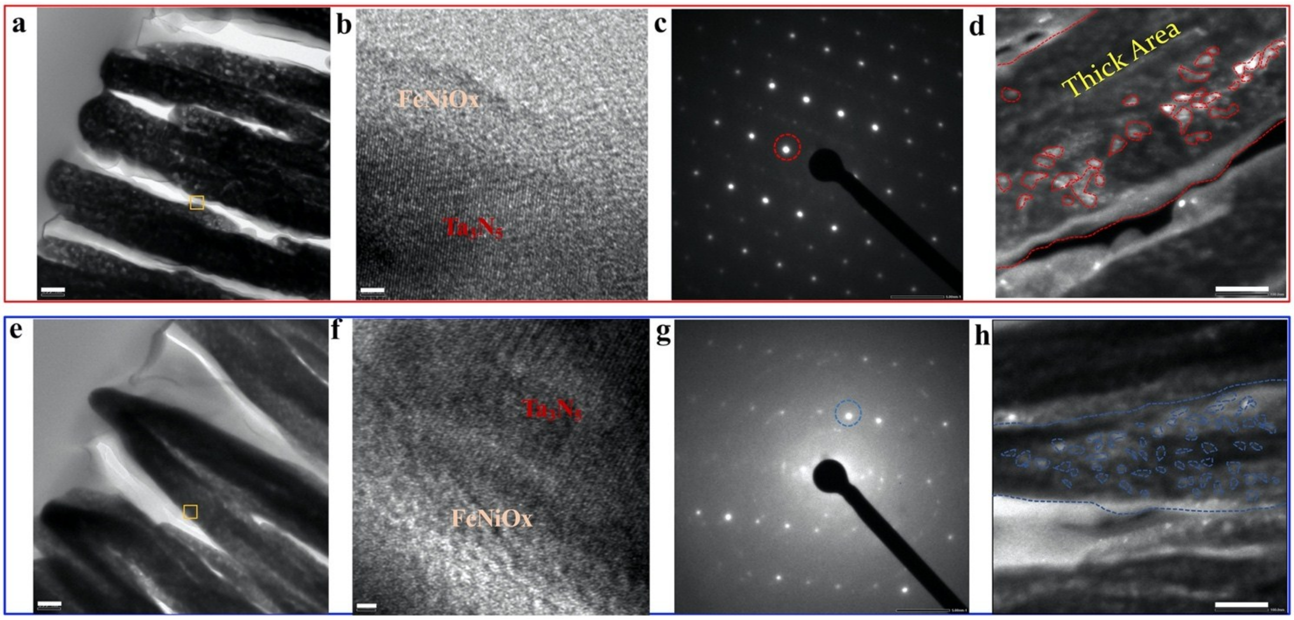

Figure S16. Transmission electron microscopy (TEM) analysis for the optimised and non-optimised Ta_3N_5-NRs/$FeNiO_x$-based photoanodes after stability test. High resolution transmission electron microscopy images of optimised (a–b) and non-optimised (e–f) Ta_3N_5-NRs . (c and g) Selected area electron diffraction patterns acquired from the optimised (a) and non-optimised (e) Ta_3N_5-NRs. Dark field images for the optimised (d) and non-optimised (h) Ta_3N_5-NRs.. Scale bars, (a, e) 100 nm, (b, f) 2 nm and (d, h) 100 nm.

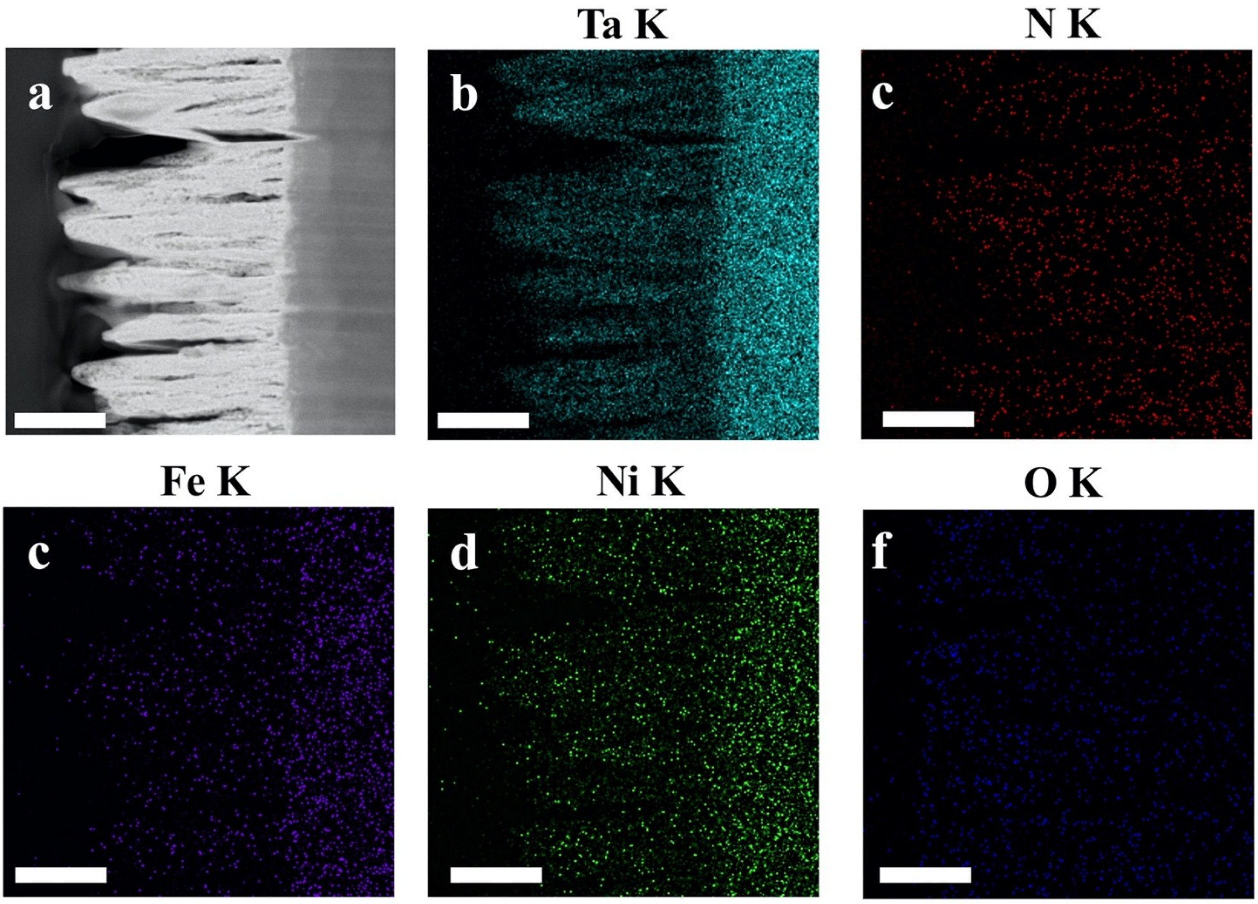

Figure S17. STEM-EDS analyses for optimised Ta/Ta_3N_5-NRs/$FeNiO_x$ after stability test. (a) TEM cross-sectional view image of the Ta_3N_5-NRs/$FeNiO_x$ photoanode. STEM-EDS elemental mapping of the area in (a) for Ta, N, Fe, Ni and O.

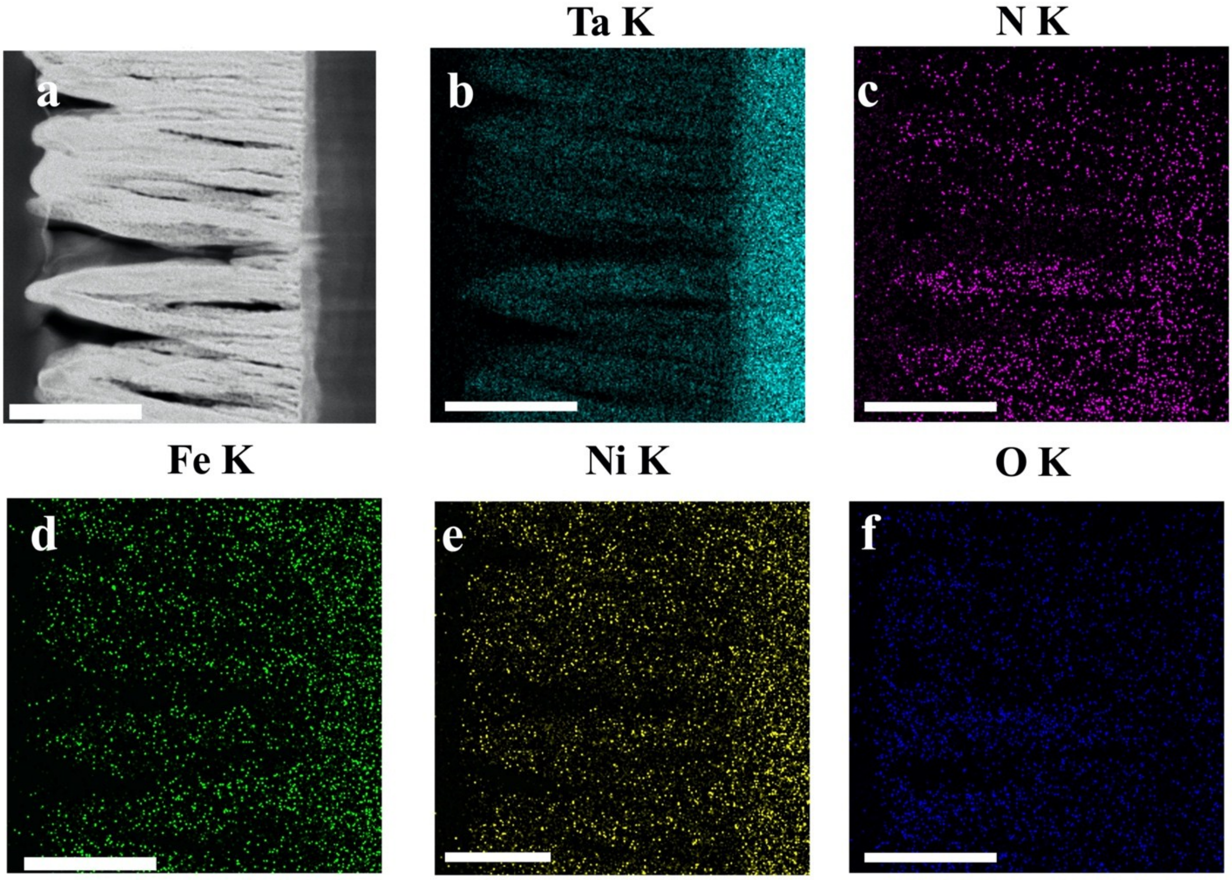

Figure S18. STEM-EDS analyses for non-optimised Ta/Ta_3N_5-NRs/$FeNiO_x$ after stability test. (a) TEM cross-sectional view image of the Ta_3N_5-NRs/$FeNiO_x$ photoanode. STEM-EDS elemental mapping of the area in (a) for Ta, N, Fe, Ni and O.

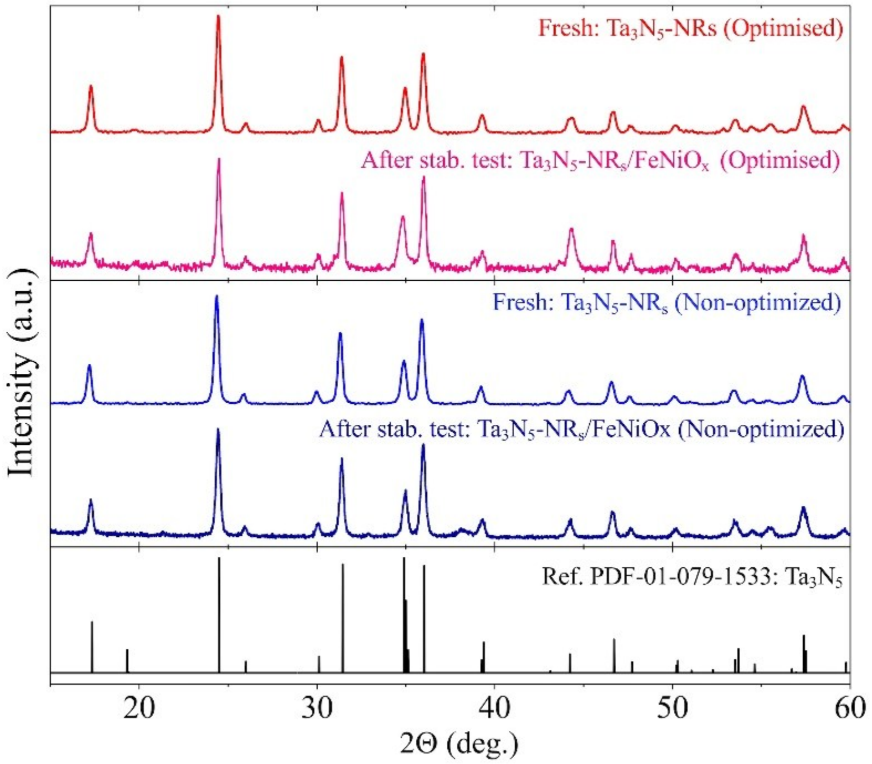

Figure S19. XRD patterns of optimized and-non optimized Ta_3N_5-NRs based samples, including the fresh ones and after PEC stability test at $1.1V_{RHE}$.

After stability test, no change in bulk composition of Ta_3N_5-NRs for both samples are observed from XRD pattern.

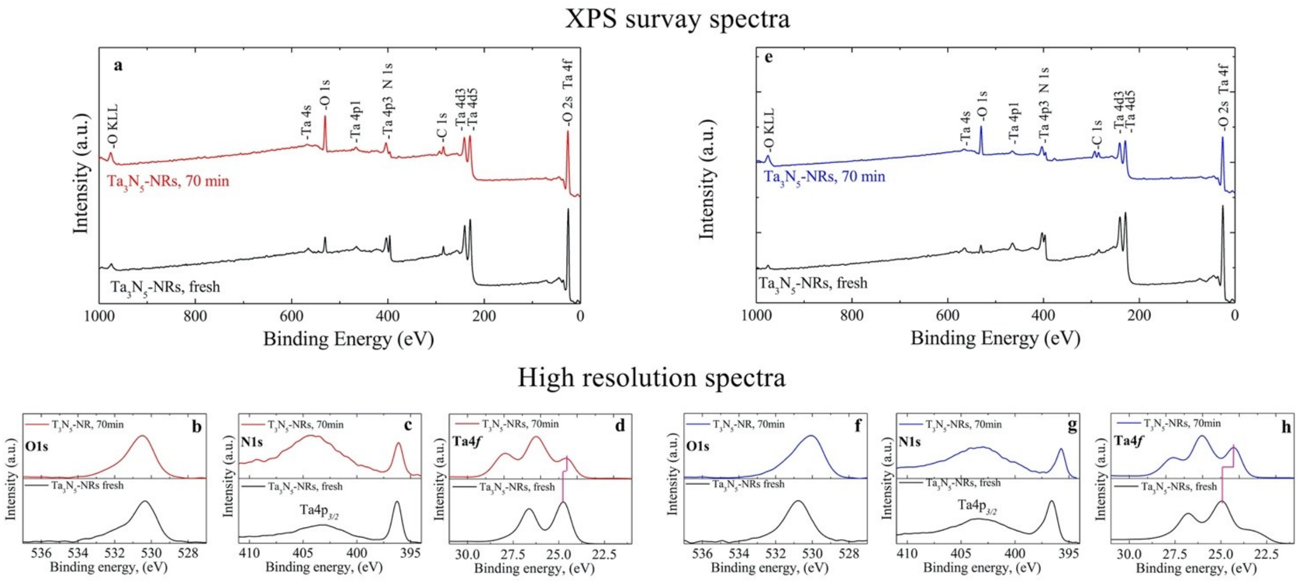

Figure S20. X-Ray photoelectron spectra (XPS) for the both optimized (a-d) and non-optimised (e-h) samples before (black lines) and after stability test (70 min).

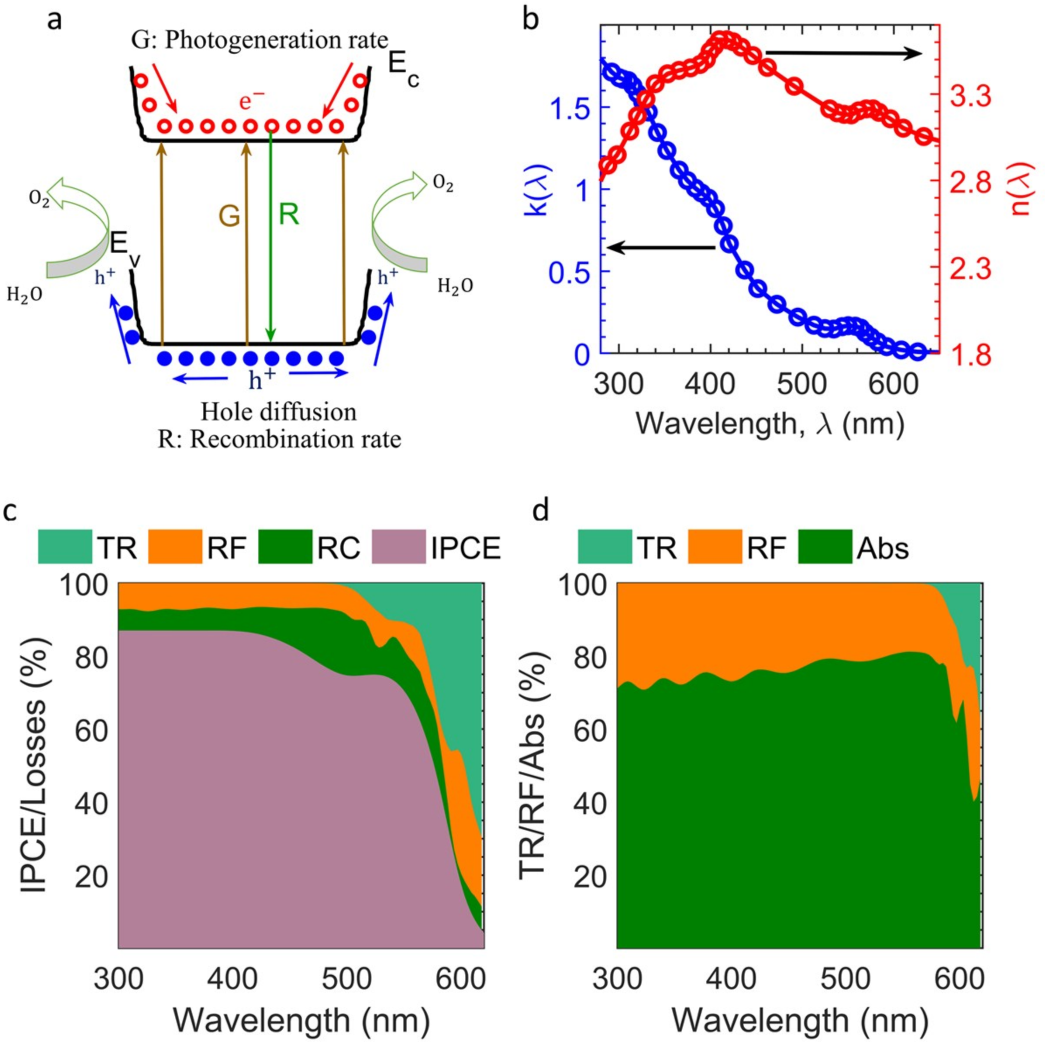

Figure S21. Optical simulations of Ta_3N_5-NRs- and thin-film (TF)-based photoanodes. (a) charge carrier dynamics in Ta_3N_5-NR photoanode. Here, E_c and E_v are the calculated conduction and valence band variation along 1-D perpendicular cut at L=1800 nm from Ta substrate. Light absorption leads to the generation of charge carriers which may recombines in the bulk of NR (depending on the carrier life time). Photogenerated holes and electrons diffused towards the surface of NR and Ta substrate, respectively. Diffused Holes at NR surface are extracted by FeNiOx cocatalyst to generate oxygen gas by water oxidation. (b) Complex refraction index (extinction coefficient *k*, refractive index *n*) of Ta_3N_5 used for optical calculations of glass/electrolyte/Ta_3N_5-NR- or TF/Ta-based photoanodes. The data is provided by the authors of ref.[6] (c) Mapping of optical (transmission TR, reflection RF), and recombination RC losses along with IPCE (for OER) of the Ta_3N_5-NR photoanode. Note that the recombination loss RC is defined as the mismatch between light absorption (Abs) and IPCE. (d) Mapping of optical losses and light absorption of Ta_3N_5-TF-based photoanode across the given wavelength spectrum. The results indicate that the scattering effect in the NR structure reduces the reflection loss RF compared with the TF device structure.

Table S1. Material parameters employed for electrical simulations of Ta_3N_5-NR-based photoanode.

Parameters, symbols	Numerical values
Effective density of states - conduction and valence band, $N_c = N_v = N$	$10^{20}\ cm^{-3}$ (ref. [6])
Charge carrier mobility, $\mu_n = \mu_p = \mu$	$1.3\ cm^2V^{-1}s^{-1}$ (ref. [7])
Dielectric constant, k	17 (ref. [7])
Donor density, N_d	$3.8 \times 10^{19} cm^{-3}$ (ref.[6])
Energy band gap, E_g	$2.1\ eV$
Electron affinity, χ	$3.92\ eV$ (ref.[8])
Charge carrier lifetime, $\tau_n = \tau_p = \tau$	$1.36\ ns$ *
Surface recombination velocity of holes, S_h	0.1 cm/s *
Work function of Schottky Contact, W_{el}	4.275 eV
Area normalised series resistance, R_s	$12\ m\Omega\ cm^2$ *

*Estimated values obtained from the calibration of simulation data with experimental data of current potential characteristics of Ta_3N_5-NR/Ta photoanode.

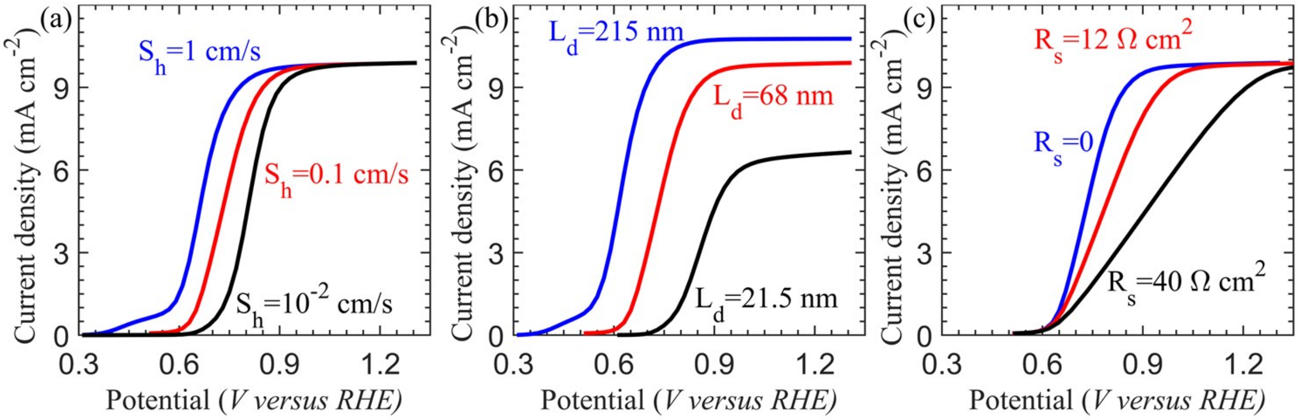

Figure S22. Electrical simulations of Ta_3N_5-NR-based photoanode. (a) Effect of surface reaction rate or surface recombination velocity of holes S_h, (b) charge carrier diffusion length L_d, and area normalised series resistance R_s on current potential characteristics of the Ta_3N_5-NR photoanode. The results suggest that the current density at 1.23 V_{RHE} is governed by additional carrier diffusion length or bulk recombination losses, whereas the onset potential is dictated by surface reaction rate S_h and bulk recombination loss. In addition, series resistance plays a significant role in determining the shape of the current potential characteristics. Based on this analysis, we calibrate the simulated data with the experimental data and estimate the associated parameters like S_h, carrier life time τ or L_d, and R_s.

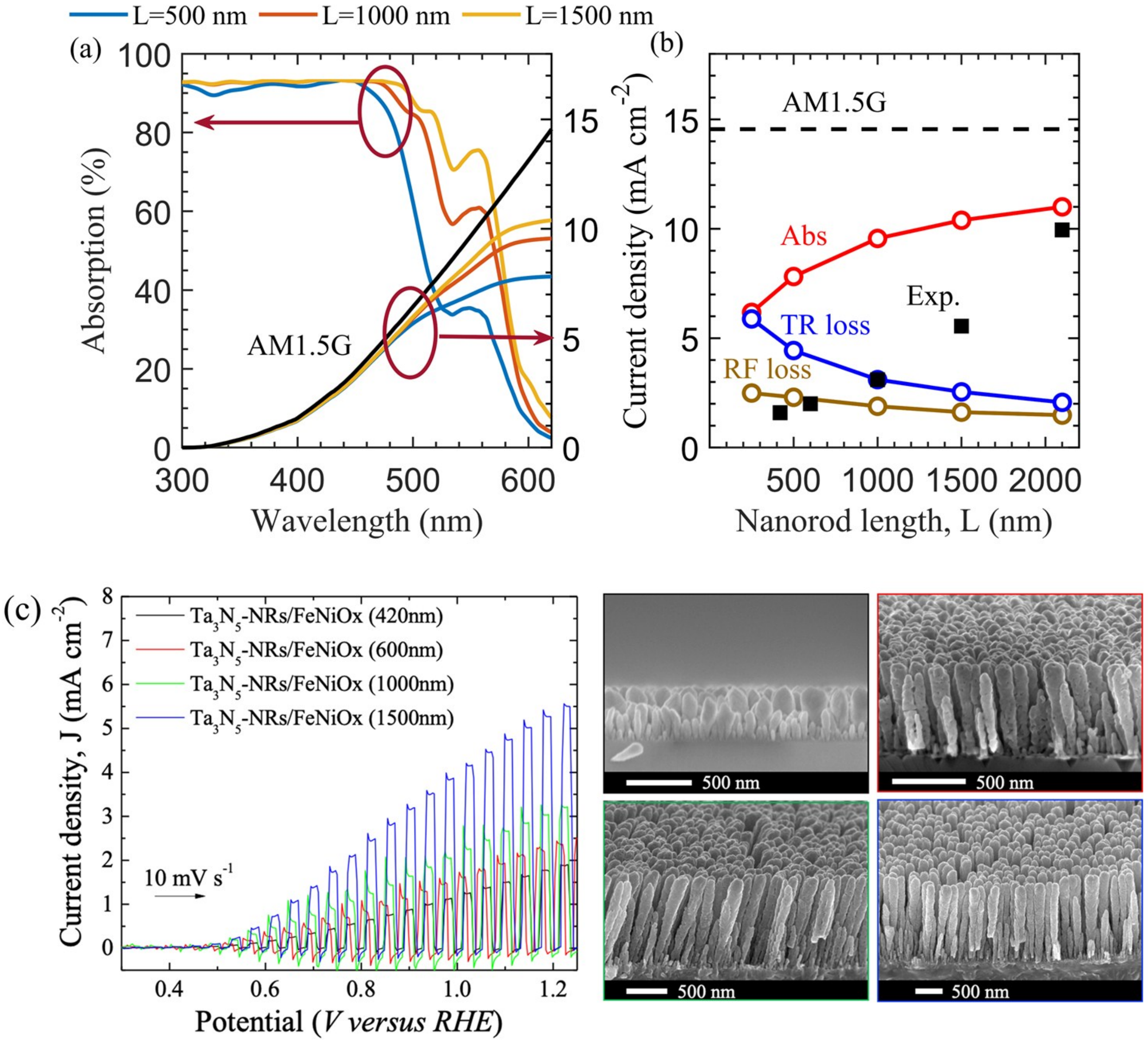

Figure S23. Effect of length of Ta_3N_5-NR son the PEC performance of Ta_3N_5-NRs based photoanodes. (a) Light absorption of modelled Ta_3N_5-NR photoanode at different NR length (L), (b) comparison of various integrated current density obtained from light absorption (Abs), reflection (RF) loss, and transmission (TR) loss at different L along with the experimental trend of photocurrent density at 1.23 VRHE with NR length of fabricated Ta_3N_5-NRs based photoanodes. (c) current potential characteristics along with SEM images of Ta_3N_5-NRs/FeNiOx based photoanodes.

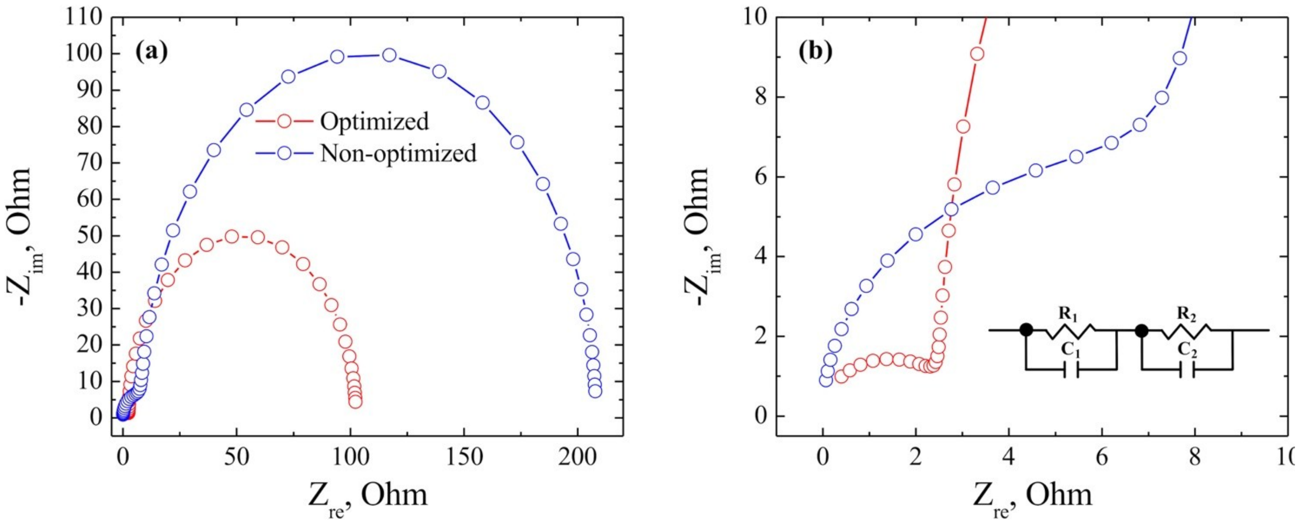

Figure S24. Nyquist plots for the optimised and non-optimised Ta/Ta_3N_5-NRs/$FeNiO_x$-based photoanodes. (a) Full range of frequencies Nyquist plots for both photoanodes measured under 1 sun of the simulated solar light at a fixed potential of 1.23 V_{RHE}. (b) Zoomed in Nyquist plots for both photoanodes at the higher frequencies range (inset scheme corresponds to the equivalent circuit used for impedance data fitting).

Table S2. Fitted impedance parameters for the optimised and non-optimised Ta/Ta_3N_5-NRs/$FeNiO_x$-based photoanodes from their corresponding Nyquist plots.

	C_1/F	R_1/Ω	C_2/F	R_2/Ω
Optimised	$5.54e^{-4}$	100	$3.67e^{-5}$	2.5
Non-optimised	$2.3e^{-4}$	200	$5.49e^{-5}$	8

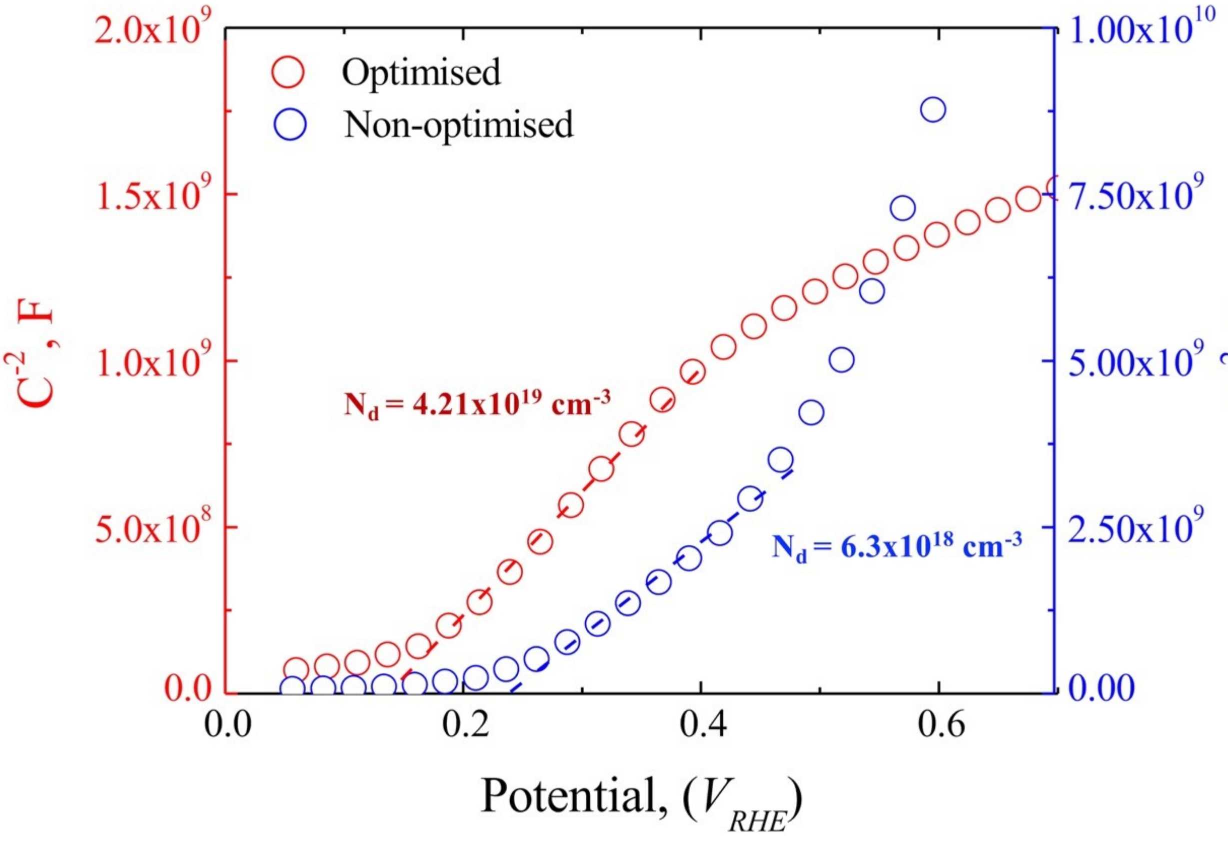

Figure S25. Mott-Schottky plots for the optimised and non-optimised Ta/Ta_3N_5-NRs-based photoanodes. Data were obtained by executing a potential scan in the anodic direction under 1000 Hz at an AC amplitude of 10 mV in 1 M of KH_2PO_4 (pH = 13) electrolyte under the dark condition. Prior to the measurements, the freshly made electrolyte was purged by argon gas under stirring for ~15 minutes. The red and blue lines show the fitting of the linear range of the Mott-Schottky plots for both the optimised and non-optimised nanorods-based photoanodes. The intercept of the fitting lines to the x-axis, corresponds to the position of the flat band potential (FBP) for both photoanodes. The FBP values for the optimised photoanode is 0.13 and that for non-optimised is 0.34 V_{RHE}. The carrier concentration (N_d) can be estimated for both photoanodes by using the following equation:

$N_d=2/(\varepsilon\varepsilon_o e k_{MS} f_r^2)$,

where ε is vacuum permittivity, ε_o is the dielectric constant of Ta_3N_5, e is the electron charge, k_{MS} is the slope of the Mott-Schottky fitting lines and f_r is the roughness factor of the Ta_3N_5 nanorods. The f_r of Ta_3N_5-NRs was estimated using *Image J* processing from the top and cross-sectional SEM images of both photoanodes, and these values were: optimised ~15.2, non-optimised ~12.8. The average nanorods diameter, length and areal nanorods density were estimated for both the optimised and non-optimised photoanodes: optimised ~120 (±10) nm, 2100 nm and 1.2×10^{9} cm^{-2}; non-optimised ~210 (±20) nm, 2100 nm and 8.2×10^{8} cm^{-2}. Finally, N_d values were estimated for both photoanodes and the results are shown in the same figure.

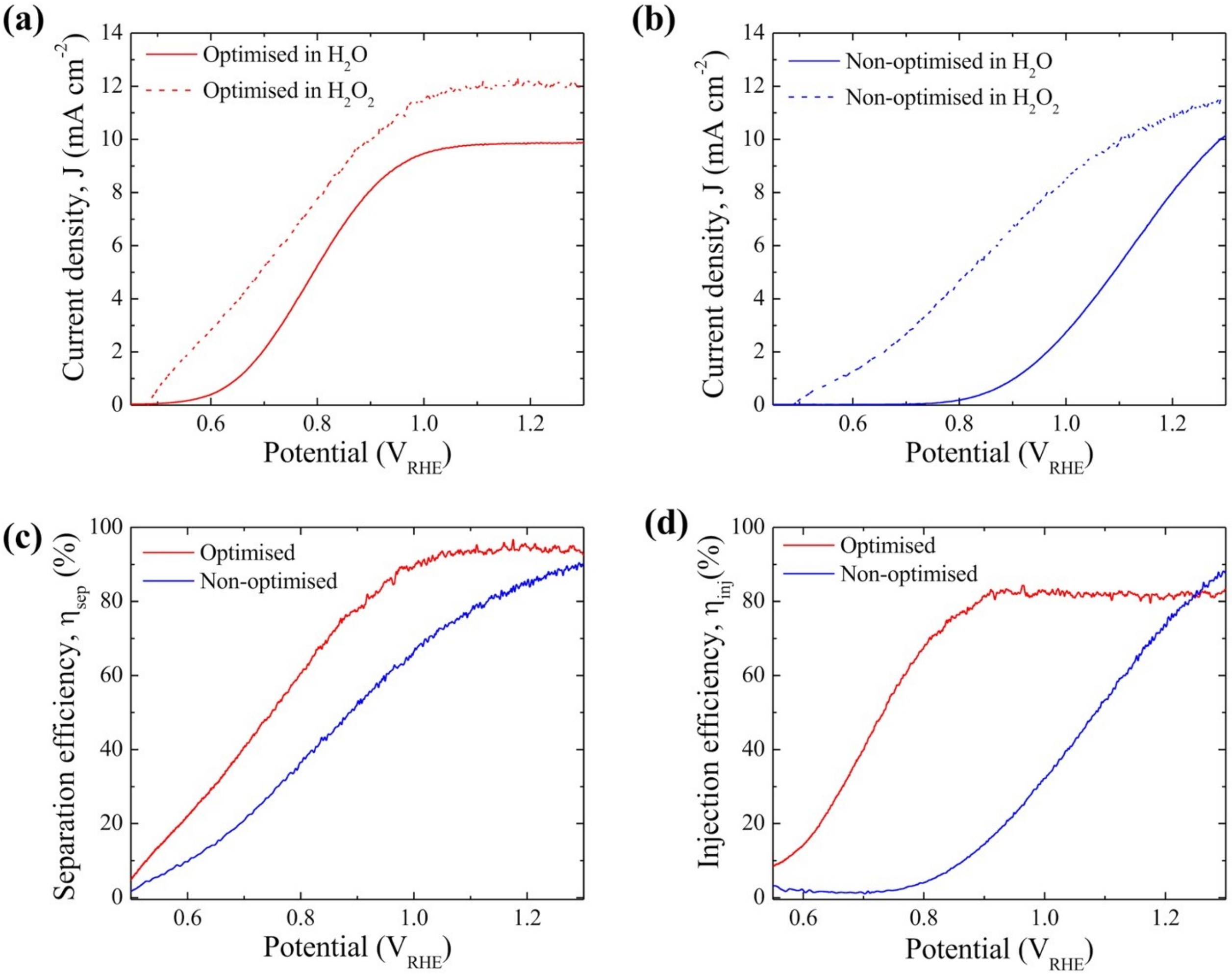

Figure S26. Separation and injection efficiencies of the optimised and non-optimised Ta_3N_5-NRs/$FeNiO_x$-based photoanodes. (a) and (b) J-V_{RHE} characteristics of the optimised and non-optimised Ta_3N_5-NRs/$FeNiO_x$ photoanodes measured in 1 M of KH_2PO_4 (pH 13) electrolyte (red and blue solid lines) and in 1 M of KH_2PO_4 + 0.5 H_2O_2 (pH 13) electrolyte (red and blue dash lines), respectively, under AM1.5G sunlight. J-V_{RHE} curves were acquired by sweeping the potential from cathodic to anodic directions at a scan rate of 10 mV s^{-1}. (c) and (d) Estimated separation and injection efficiencies for both the optimised and non-optimised photoanodes.

The separation (η_{sep}) and injection (η_{inj}) efficiencies characterise bulk and surface recombination processes. According to Dotan et. al.[9] the water splitting photocurrent can be described as: $J^{H2O}=J_A\times\eta_{sep}\times\eta_{inj}$ (1)

where, η_{sep} is the yield of the photogenerated holes that reach to the electrode/electrolyte interface (i.e., the fraction of holes that does not recombine with the electrons in the bulk). η_{inj} is the yield of the photogenerated holes which are reached to the electrode/electrolyte interface , inject into the electrolyte to oxidise water (i.e., the fraction of holes that does not recombine with electrons at surface traps). J_A is the integrated current density obtained from the product of photon absorption and AM1.5G solar spectrum irradiance. . An independent estimation of η_{sep} and η_{inj} is possible by measuring the photoanode photocurrent J^{H2O2} in the electrolyte that contains a hole scavenger (e.g., H_2O_2). This method assumes that the hole scavenger removes the injection barrier to realise 100% of η_{inj} ($\eta_{inj} = 1$) without affecting bulk recombination process of electrode i.e. η_{sep}. Therefore, J^{H2O2} photocurrent can be estimated as follow:

$J^{H2O2} = J_A \times \eta_{sep}$ (2)

Based on equation (1) and (2), the injection and separation efficiencies can be express as:

$\eta_{inj} = J^{H2O}/J^{H2O2}$ (3)

$\eta_{sep} = J^{H2O2}/J_A$ (4)

In our case, both photoanodes in the presence of H_2O_2 reached the photocurrent density of ~12 mA cm^{-2} at 1.23 V_{RHE}. To calculate separation efficiency, we assumed that J_A is the theoretical maximum photocurrent value of 12.9 mA cm^{-2} This assumption of J_A to calculate separation efficiency is previously reported in the literature[10].

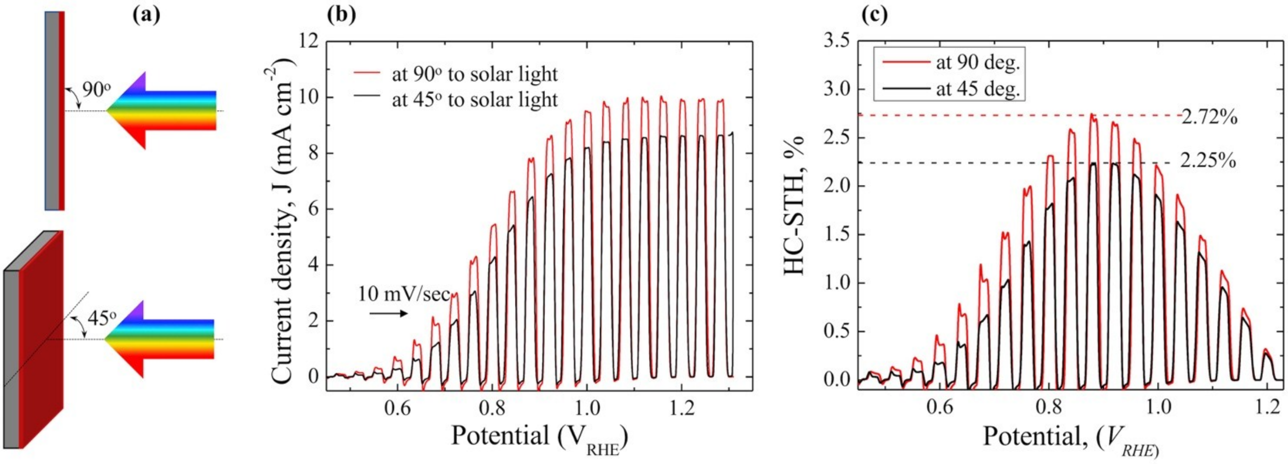

Figure S27. PEC properties of the optimised photoanode measured at different incident angles. (a) Schematic illustration of the light incident angle to the photoanode. (b) Comparison of *J*-*V* characteristics measured at incident angles of 90° and 45° for the optimised Ta_3N_5-NRs/FeNiO$_x$-based photoanode and (b) the corresponding calculated HC-STH.

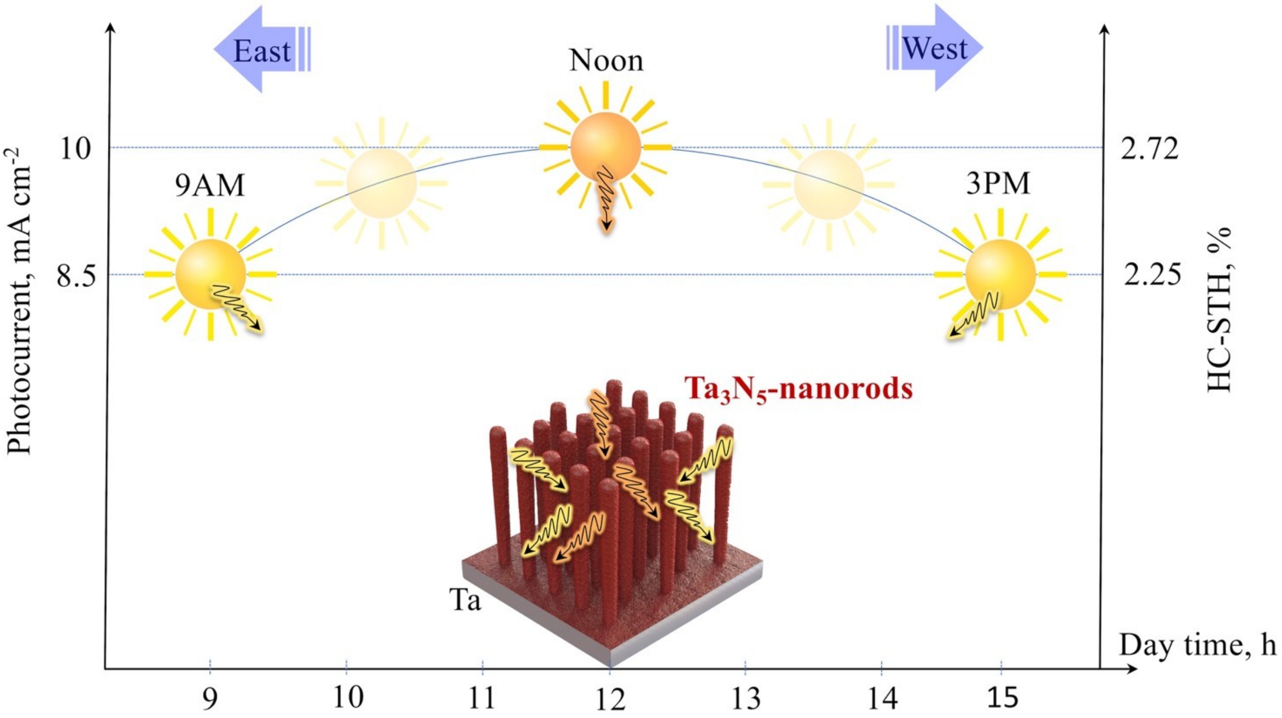

Figure S28. Projection of the daily sun movement on HC-STH efficiency for the Ta_3N_5-NRs-based photoanode.

Table S3. Recent report on the state-of-the-art efficiencies for single-photon photoanodes (2013–2020).

Year	Material, Structure	Photocurrent at 0.9 V_{RHE} (mA/cm^2)	Photocurrent at 1.23 V_{RHE} (mA/cm^2)	HC-STH (%)
Current	Ta_3N_5-NRs/FeNiOx	8.2	9.95	2.72@0.89 V_{RHE}
[6]2019	Transparent photoanode: Al_2O_3/GaN/Ta_3N_5 film/FeNiOx	~3.5	6.3	1.15@0.94 V_{RHE}
[11]2018	Single crystalline Ta_3N_5-polyhedron/$Ni_{0.9}Fe_{0.1}OOH$	~2.2	5.6	NA
[12]2017	Ta_3N_5 film/GaN film/Co-Pi	~4.3	8	1.5
[13]2016	Ta_3N_5 film/TiOx/Fh/Ni(OH)$_x$/complex 1/complex 2	~7.7	12.1	2.5@0.9V_{RHE}
[14]2015	N_2-treated $BiVO_4$/FeOOH/NiOOH	~4.2	4.8	2.2@0.6V_{RHE}
[15]2014	$BiVO_4$/FeOOH/NiOOH	~3.5	4.4	1.75@0.6V_{RHE}
[16]2013	Ba:Ta_3N_5 -NRs/ Co-Pi	~4.5	6.7	1.5@0.87V_{RHE}

NR_s-nanorods

References

1 K. Robbie and M. J. Brett, *J. Vac. Sci. Technol. A Vacuum, Surfaces Film.*, 1997, **15**, 1460–1465.

2 Y. Pihosh, I. Turkevych, K. Mawatari, N. Fukuda, R. Ohta, M. Tosa, K. Shimamura, E. G. Villora and T. Kitamori, *Nanotechnology*, 2014, **25**, 315402.

3 Y. Pihosh, I. Turkevych, K. Mawatari, J. Uemura, Y. Kazoe, S. Kosar, K. Makita, T. Sugaya, T. Matsui, D. Fujita, M. Tosa, M. Kondo and T. Kitamori, *Sci. Rep.*, 2015, **5**, 11141.

4 Y. Pihosh, I. Turkevych, K. Mawatari, T. Asai, T. Hisatomi, J. Uemura, M. Tosa, K. Shimamura, J. Kubota, K. Domen and T. Kitamori, *Small*, 2014, **10**, 3692–3699.

5 N. P. Poluektov, Y. P. Tsar'gorodsev, I. I. Usatov and A. G. Evstigneev, *Thin Solid Films*, 2017, **640**, 60–66.

6 T. Higashi, H. Nishiyama, Y. Suzuki, Y. Sasaki, T. Hisatomi, M. Katayama, T. Minegishi, K. Seki, T. Yamada and K. Domen, *Angew. Chemie - Int. Ed.*, 2019, **58**, 2300–2304.

7 A. Ziani, E. Nurlaela, D. S. Dhawale, D. A. Silva, E. Alarousu, O. F. Mohammed and K. Takanabe, *Phys. Chem. Chem. Phys.*, 2015, **17**, 2670–2677.

8 W. J. Chun, A. Ishikawa, H. Fujisawa, T. Takata, J. N. Kondo, M. Hara, M. Kawai, Y. Matsumoto and K. Domen, *J. Phys. Chem. B*, 2003, **107**, 1798–1803.

9 H. Dotan, K. Sivula, M. Grätzel, A. Rothschild and S. C. Warren, *Energy Environ. Sci.*, 2011, **4**, 958–964.

10 L. Pei, B. Lv, S. Wang, Z. Yu, S. Yan, R. Abe and Z. Zou, *ACS Appl. Energy Mater.*, 2018, **1**, 4150–4157.

11 Z. Shi, J. Feng, H. Shan, X. Wang, Z. Xu, H. Huang, Q. Qian, S. Yan and Z. Zou, *Appl. Catal. B Environ.*, 2018, **237**, 665–672.

12 M. Zhong, T. Hisatomi, Y. Sasaki, S. Suzuki, K. Teshima, M. Nakabayashi, N. Shibata, H. Nishiyama, M. Katayama, T. Yamada and K. Domen, *Angew. Chemie - Int. Ed.*, 2017, 56, 4739–4743.

13 G. Liu, S. Ye, P. Yan, F. Xiong, P. Fu, Z. Wang, Z. Chen, J. Shi and C. Li, *Energy Environ. Sci.*, 2016, **9**, 1327–1334.

14 T. W. Kim, Y. Ping, G. A. Galli and K. S. Choi, *Nat. Commun.*, 2015, **6**, 1–10.

15 T. W. Kim and K. S. Choi, *Science (80-.).*, 2014, **343**, 990–994.

16 Y. Li, L. Zhang, A. Torres-Pardo, J. M. González-Calbet, Y. Ma, P. Oleynikov, O. Terasaki, S. Asahina, M. Shima, D. Cha, L. Zhao, K. Takanabe, J. Kubota and K. Domen, *Nat. Commun.*, 2013, **4**, 1–2.